# 3D FE Analysis of Monotonic Undrained Hollow Cylinder Torsional Shear Test considering Specimen Geometries

XU, Binbin [1], NAKAI, Kentaro [2], NODA, Toshihiro [3]

1 Nagoya University・Department of Civil Engineering・xu@soil.civil.nagoya-u.ac.jp
2 Nagoya University・Department of Civil Engineering
3 Nagoya University・Department of Civil Engineering

## ABSTRACT

Hollow cylinder torsional shear test is simulated regarded as a boundary value problem employing a 3D static/dynamic soil-water coupled finite deformation analysis to investigate the influence of the specimen geometries on apparent behavior concerned in practical experiments. 1) As for the specimen geometries, a new evaluating method for the non-uniformity inside the specimen is proposed which is suitable for 3D deformation and can represent not only the influence of curvature but also the effect of end constraints. 2) A “Perfect path” which means the response of a single 3D element with uniform deformation is calculated to investigate the effect of non-uniformities on the apparent behavior. As can be seen, only the apparent behavior with thinnest wall thickness coincides with the “Perfect path”, which indicates a uniform deformation inside the thinnest specimen. 3) There is a sudden relaxation in the deviator stress in the specimen with H/D=2.5, which indicates that even if larger heights of specimen can reduce the end constraints, there is still a critical ratio of height and diameter to prevent end failure in advance. 4) Even thought the non-uniformity in different geometries is quite different, there seem to be no significant influence on the apparent behavior. The reason may lie in the extreme constraint conditions, namely displacement control.

Keywords: three-dimension, non-uniformity, specimen geometries, apparent behavior

## 1. Introduction

In practical geotechnical engineering, grounds/soils are generally under a complex stress state and subjected to various loading conditions. In order to grasp strengthening and deformation properties of the ground, many laboratory testings were developed and conducted. Among them, the hollow cylinder torsional shear test controlled by four individual external forces is often employed in order to reproduce the actual stress path during in-situ constructions. Via adjusting the loading condition, the soil response can be investigated under the designated stress path by both monotonic and cyclic shear tests. **Fig. 1** presents a sketch of the specimen. $F_z$, $T_\theta$, $P_o$ and $P_i$ represent the vertical load, torque and external and internal pressures respectively, which will result in stresses including $\sigma_{zz}$, $\sigma_{rr}$, $\sigma_{\theta\theta}$ and $\sigma_{\theta z}$ for every element in the sample and four induced strains consisting of $\varepsilon_{zz}$, $\varepsilon_{rr}$, $\varepsilon_{\theta\theta}$ and $\varepsilon_{\theta z}$ in each corresponding direction. Details can be seen in **Appendix-A**.

Since the new experiment apparatus was introduced by Height et al. [1)], a lot of literatures 2), 3), 4) have discussed about the influences of initial anisotropy, intermediate principal stress, direction of principal stresses and rotation of principal stresses on soil strength and deformation. Meanwhile, as indicated by Height et al., the non-uniformities of stress and strain would be caused due to both the curvature of the cylinder wall and the end constraints and an evaluating index which is related to the sample geometry, stress path and constitutive

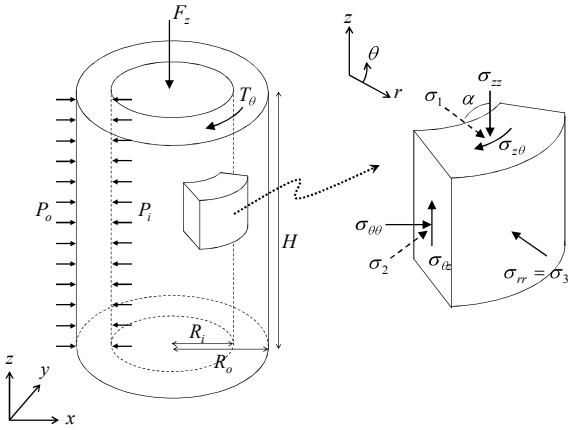


**Fig. 1** Sketch of HCT test and stress state

model was defined to quantify the level of non-uniformities. Lade [5] conducted a series of hollow torsional experiments with different specimen heights to eliminate the effect of friction at the end. Sayao and Vaid [6], based on the assumption of Height, proposed a more rigorous index for the non-uniformities inside the sample and discussed the influence factors including stress ratio, specimen height, diameter and wall thickness by the assumption of a non-linear constitutive model.

In order to check the influence of non-uniform deformation during numerical calculations, it is reasonable to treat the analysis of specimen as boundary value problems (hereafter noted as BVPs) instead of one element response. The deformation of specimen was described as BVPs under axial-symmetric and plane strain conditions by Asaoka et al.[7),8)] and it was found that there were remarkable water migration and obvious strain localization and the apparent behavior deviated from the one element behavior, which is quite different from the response of one element under uniform deformation. Xu et al.[9)] modeled a conventional triaxial monotonic compression test under the three dimensional condition utilizing the same method and focused on the influence of loading rates on the geometry changes. Jin et al.[10)] dealt with a series of cyclic triaxial tests numerically and demonstrated the results by changing the cyclic loading frequencies, confining pressures and so on. But for the numerical simulation of hollow torsional tests, since Gens and Potts [11)] presented a quasi-axisymmetric BVP by finite element analysis, where they expressed non-axisymmetric forces and/or displacements as Fourier series in the circumferential directions, to show the non-uniformity of stress along the wall thickness, there are few literatures concentrating on the simulation of hollow torsional tests.

Therefore, to succeed the study of BVPs and fill the gap of numerical simulation in hollow torsion tests, this paper intends to treat the monotonic undrained hollow cylinder shear test as a three-dimension boundary value problem to reevaluate non-uniformity because of sample geometries and end constraints by a more efficient constitutive model---SYS Cam clay model[12),13)] and a dynamic soil-water coupled finite deformation analysis code[14),15)], and to establish a basic thought for further monotonic and cyclic loading conditions under more complex stress paths.

## 2. Calculation conditions

The specimen as a benchmark is with a height of 8 cm, inner diameter of 4 cm and outer diameter of 8 cm as shown in Fig. 2. The division in radial, circumferential and vertical directions is 5×32×20 with totally 3200 elements and 4032 nodes. For the mechanical boundary conditions, all the nodes at the bottom surface are fixed in *x*, *y* and *z* directions and a constant angular velocity 0.005 rad/s, namely 0.1875%/s is applied to each node on the top surface. Except the internal and external pressures, there is no additional vertical load, namely $F_z$=0 in the vertical direction at the top surface. Equal external and internal pressures are set up. Hereafter, if there is no additional specification, the above boundary condition is adopted preferredly. Therefore, $\sigma_{rr}$ is regarded as the intermediate principal stress and the coefficient of intermediate principal stress $b$ is 0.5. The angle between orientation of maximum principal stress and the vertical orientation is constantly 45 degree. For the hydraulic boundary condition, the entire boundary is assumed to be impermeable.

Typical saturated clay with a relatively low permeability is employed in the analysis and the detailed elasto-plastic parameters and initial values are presented in **Table 1**, from which it can be seen it is non-structured overconsolidated clay. The sample is firstly consolidated to 1467 kPa and then unloaded to 294.3 kPa isotropically. Gravitational influence is not considered in the analysis and initial values are regarded to be uniform in the vertical direction.

**Table 1** Soil parameters and initial conditions

| *Elasto-plastic parameters* | | *Initial conditions* | |
|---|---|---|---|
| Critical state index M | 1.55 | Specific volume $v_0$ | 1.747 |
| NCL intercept N | 2.0 | Stress ratio $\eta_0$ | 0.0 |
| Compression index $\tilde{\lambda}$ | 0.108 | Degree of structure $1/R_0^*$ | 1.0 |
| Swelling index $\tilde{\kappa}$ | 0.025 | Degree of overconsolidation $1/R_0$ | 5.0 |
| Poisson's ratio $\nu$ | 0.3 | Degree of anisotropy $\varsigma_0$ | 0.0 |
| *Evolution parameters* | | Soil particle density $\rho_s$ (g/cm$^3$) | 2.65 |
| Degradation index of OC m | 0.2 | Coefficient of permeability $k$ (cm/s) | $3.7 \times 10^{-8}$ |

## 3. Calculation results

### 3.1 A three-dimension Finite Element Result

First a benchmark result is presented under displacement control to demonstrate the distribution of the shear strain, excess pore water pressure and overconsolidation.

**Fig. 2**(a) indicates the deformation mode (3D shear strain distribution) as the apparent shear strain $\gamma_s$ increases. Note that the apparent shear strain is acquired by $\gamma_s = (R_o + R_i) \times \Delta\theta/(2H)$, where $\Delta\theta$ is measured at the node located at the average of inner and outer radius on the top surface, while the shear strain in the contour means the Eulerian strain calculated from the current configuration. It is revealed that the torsional deformation is represented in the vertical direction which is similar to that in practical experiments as shown in **Fig. 2**(b). **Figs. 3 and 4** indicate the distributions of excess pore water pressure and overconsolidation on the cross section of *x*-*z* plane at different apparent shear strains. As predicted theoretically by the linear elastic model[1)], there is a remarkable non-uniformity of shear strain along the radius. Benefiting from the soil-water coupled analysis and SYS-Cam clay model, the non-uniformities of excess pore water pressure and

overconsolidation are also newly observed. And all of the non-uniformities become severer/wider with the increase of apparent shear strain.

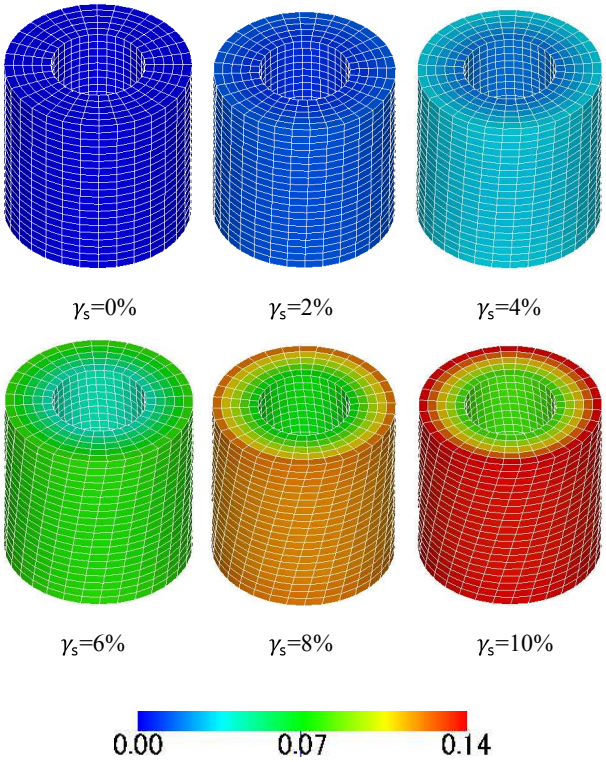


(a) Simulation result

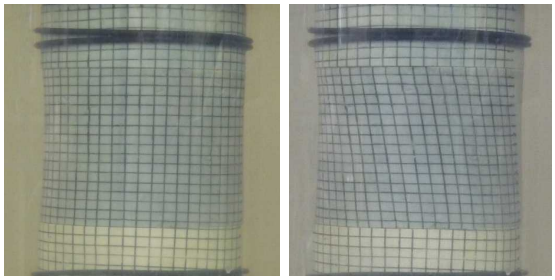


(b) Experiment result

**Fig. 2** Comparison of deformation mode between numerical and experimental results

### 3.2 Influence of specimen geometries

As mentioned initially, the non-uniformities in stress and strain mainly come from the curvature of cylinder wall and the friction due to constraints at the end. To reduce such non-uniformities, in the practical experiments the thinner wall thickness, the larger inner and outer diameters and the greater height are recommended. Before evaluating the influence of non-uniformities on the apparent behavior, a response under completely uniform deformation is calculated by modelling a single 3D eight-node element with unit dimensions to act as a benchmark. The boundary conditions are set to be exactly same as the right element shown in Fig. 1. Details can be seen in **Appendix-B**. Meanwhile, as shown above now that the non-uniformities in shear strain, specific volume change are so significant, how to quantify such non-uniformities is essential.

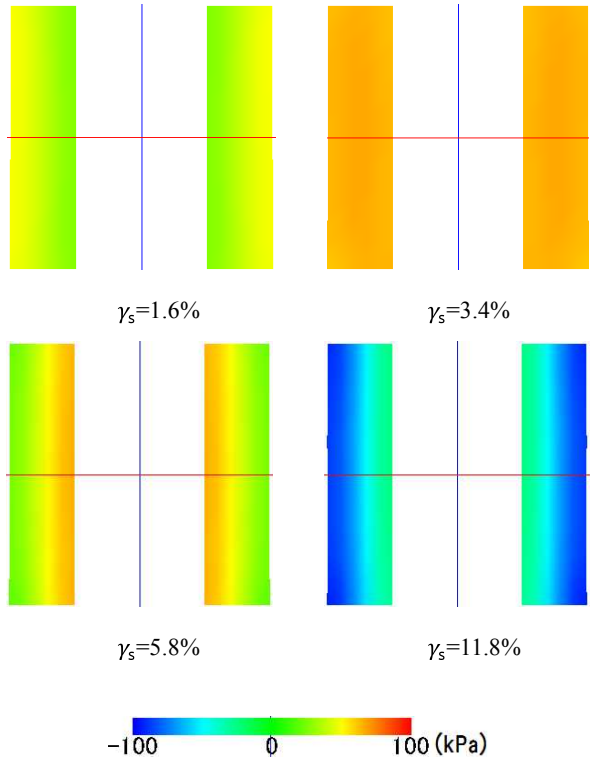


**Fig. 3** Distribution of excess pore water pressure at *x*-*z* cross section

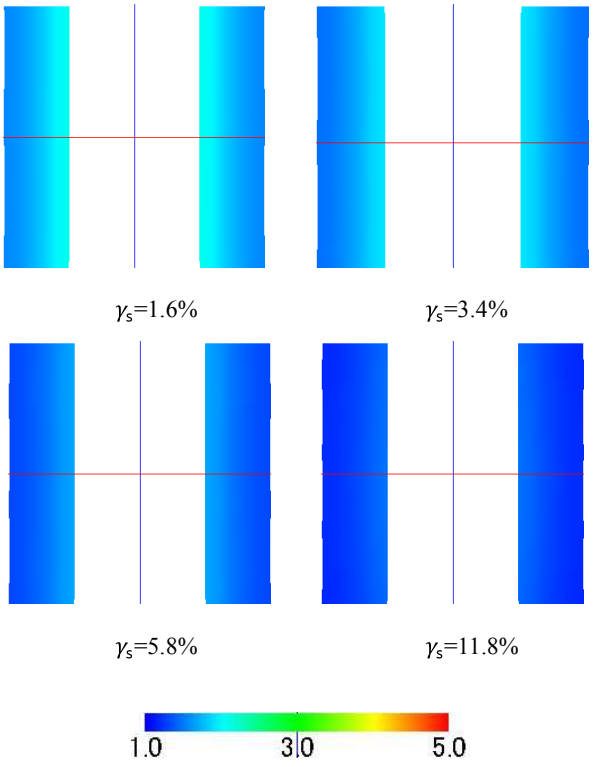


**Fig. 4** Distribution of overconsolidation at *x*-*z* cross section

Height et al.[1] defined a coefficient $\beta_3$ for each individual stress to evaluate the non-uniformity of radial direction:

$$\beta_3 = \frac{1}{(R_o - R_i)} \frac{1}{\sigma_L} \int_{R_i}^{R_o} |\sigma(r) - \bar{\sigma}| dr$$

where $\sigma(r)$ is the individual stress including $\sigma_{rr}$, $\sigma_{\theta\theta}$ and $\sigma_{\theta z}$, $\bar{\sigma}$ is the average value of the corresponding stress and $\sigma_L$ is the standard stress taken as $\bar{\sigma}_{\theta z}$ for $\sigma_{\theta z}$ and $1/2(\bar{\sigma}_{\theta\theta} + \bar{\sigma}_{rr})$ for $\sigma_{rr}$ and $\sigma_{\theta\theta}$. Sayao and Vaid [5] proposed another evaluating coefficient $\beta_\eta$ viewed from the stress ratio:

$$\beta_\eta = \frac{\eta_{max} - \eta_{min}}{\bar{\eta}}$$

where $\eta_{max}$, $\eta_{min}$ and $\bar{\eta}$ are maximum, minimum and average stress ratios respectively.

However, both of them are proposed based on the axial-symmetry deformation, which is not suitable for three-dimension analysis. Therefore, a new variable $\Delta A$ is defined as follows to assess the non-uniformity:

$$\Delta A = \frac{\sum_{i=1}^{NE} |A(i) - \bar{A}| \cdot \Delta V(i)}{\sum_{i=1}^{NE} \Delta V(i)}$$

where

$$\bar{A} = \frac{\sum_{i=1}^{NE} A(i) \cdot \Delta V(i)}{\sum_{i=1}^{NE} \Delta V(i)}$$

here, $A(i)$ can be the mean effective stress, deviator stress, shear strain and so on within each element, $\Delta V(i)$ is the current volume for element $i$, $\bar{A}$ is the weighted average of $A(i)$ taking the volume ratio $\Delta V(i)/\sum_{i=1}^{NE} \Delta V(i)$ as the weight coefficient and $\Delta A$ is the weighted average of deviation between $A(i)$ and $\bar{A}$. $\Delta A$ has the same unit with $A(i)$. The smaller $\Delta A$ is, the more uniform $A(i)$ is. The ideal uniform distribution of $A(i)$, that is $A(i)$=const, results in $\Delta A$=0.

**Table 2** gives the calculation schemes for different specimen geometries, in which "Thic." means the cylinder wall thickness, "H" and "D" are the height and the outer diameter respectively. Take the first column "Thic." as an example, the height and outer diameter of the specimen are kept constant with only changing the wall thickness with 0.4 cm, 2 cm and 3.6 cm to investigate the influence on non-uniformities and the bold item represents the benchmark geometry described in 3.1. The remaining columns of "H" and "D" can be interpreted analogically.

**Table 2** Calculation schemes for various specimen geometries

| Geometries: | Thic. | H | D |
|---|---|---|---|
| Thickness<br>Height<br>Diameter | 0.4 cm | 2 cm | **8 cm** |
| | **2 cm** | **8 cm** | 12 cm |
| | 3.6 cm | 12 cm | 16 cm |
| | × | 20 cm | 20 cm |
| Remarks | H=8 cm<br>D=4 cm | Thic.=2 cm<br>D=4 cm | Thic.=2 cm<br>H=8 cm |

### 3.2.1 Influence of wall thickness

**Figs. 5, 6** and **7** presents the deviations of mean effective stress $p'$, stress ratio $\eta$ and shear strain $\varepsilon_s$ against the apparent shear strain. Once again, the non-uniformities of four variables increase as the wall thickness becomes larger, which proves the validity of the proposed method. The minimum deviations of mean effective stress, stress ratio and shear strain are about 6 kPa, 0.03 and 4% respectively in Thic.=0.4 cm. The maximum ones are over 30 kPa, 60 kPa, 0.25 and 2% respectively in Thic.=3.6 cm. The non-uniformity of shear strain increases linearly with the increase of apparent shear strain.

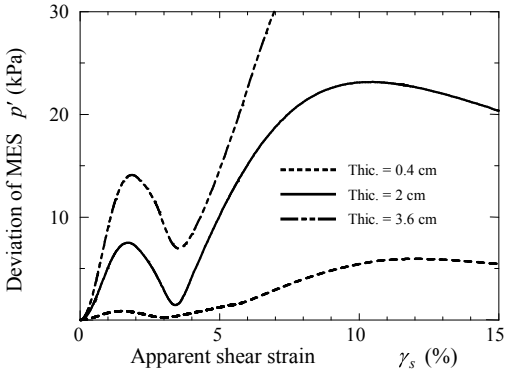


**Fig. 5** Non-uniformity of mean effective stress $p'$

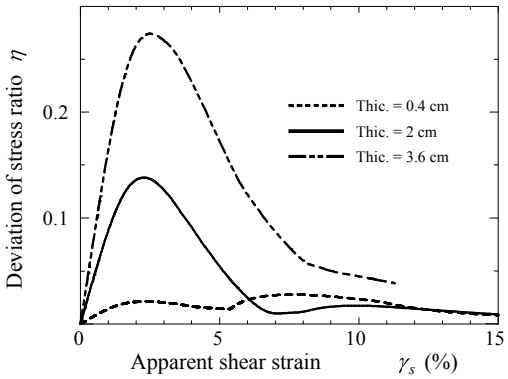


**Fig. 6** Non-uniformity of stress ratio $\eta$

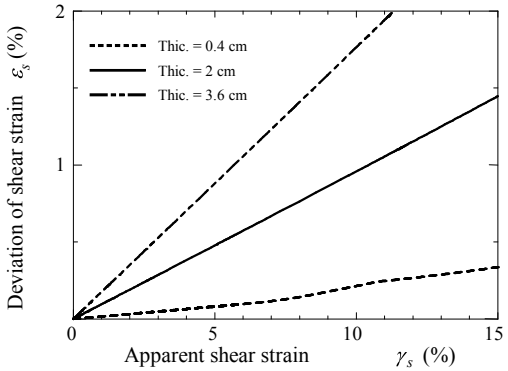


**Fig. 7** Non-uniformity of shear strain $\varepsilon_s$

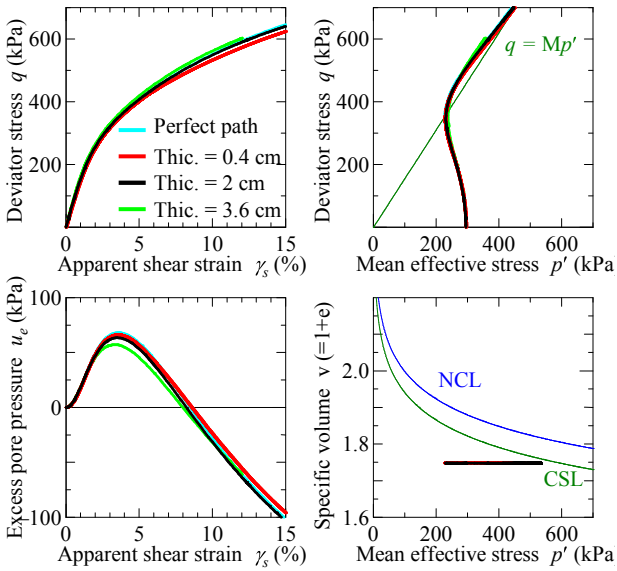


**Fig. 8** Apparent behavior for different wall thicknesses

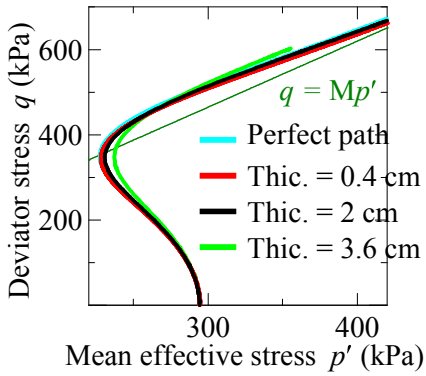


**Fig. 9** Enlargement of effective stress path

**Fig. 8** depicts the apparent behavior for three wall thicknesses comparing with the "Perfect path" that represents the response of one element mentioned at the beginning of 3.2 including deviator stress $q$ ~apparent shear strain $\gamma_s$, $q$ ~mean effective stress $p'$ (namely effective stress path), excess pore water pressure $u_e \sim \gamma_s$ and specific volume v ~ $p'$. Here, $q$ and $p'$ are derived from Eq. (A-3) in **Appendix-A**, where the torque $T_\theta$ is the sum of products of the tangential nodal force calculated at each node on the top and the corresponding radial distance. Apparent shear strain $\gamma_s$ is taken as the same method mentioned above. It should be pointed out here that different from $\sigma_{\theta z}$ directly measured step by step, $\sigma_{zz}, \sigma_{rr}$ and $\sigma_{\theta\theta}$ which are equal to the confining pressure initially in Eq. (A-1) are average values viewing from the entire specimen and maintain constant under such mechanical boundary conditions. Excess pore water pressure $u_e$ can be measured utilizing the weighted mean pore water pressure inside the elements at the top, bottom or average of top and bottom layers and here the excess pore water pressure generated at the top is adopted. As for specific volume v, the weighted average specific volume of

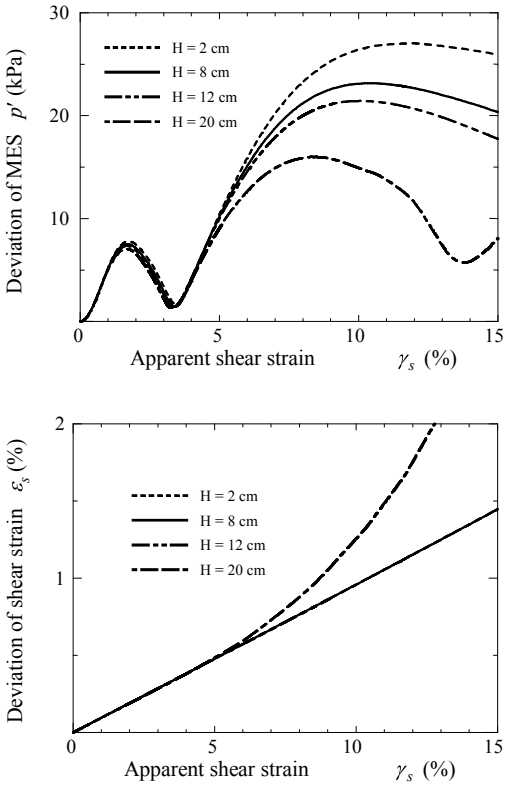


**Fig. 10** Non-uniformity of (a) mean effective stress $p'$ and (b) shear strain $\varepsilon_s$

each element is taken respect to the current configuration volume. The line $q$=$Mp'$ means the project of critical state surface on the $q$-$p'$ stress plane and NCL and CSL represent the normal consolidated line and critical state line respectively. Except the obvious lower peak in excess pore water pressure at Thic.=3.6 cm, there seems to be no else difference between the "Perfect path" and responses of three thicknesses. Note that the reason that the relationship between deviator stress and apparent shear strain differs from one another may be attributed to the measurement of apparent shear strain at different average radii for various thicknesses. It can be seen from **Fig. 9** which is the enlarged effective stress path that the thinner the cylinder wall is, the closer the effective stress path is to that in "Perfect path". However, the differences among the "Perfect path", Thic.=0.4 cm and Thic.=2 cm are so small that the result is acceptable as for Thic.=2 cm, even though the non-uniformity is quite large in **Figs. 5**, **6** and **7**.

### 3.2.2 Influence of specimen height

**Fig. 10** presents the deviations of mean effective stress and shear strain against the apparent shear strain for various heights. From the deviations of mean effective stress, it can be concluded that the non-uniformities decreases as the specimen height increases, which is in agreement with the experiment results in literature 5). Moreover, the results show that the

proposed method can deal with the non-uniformity of not only the radial direction but also the vertical direction.

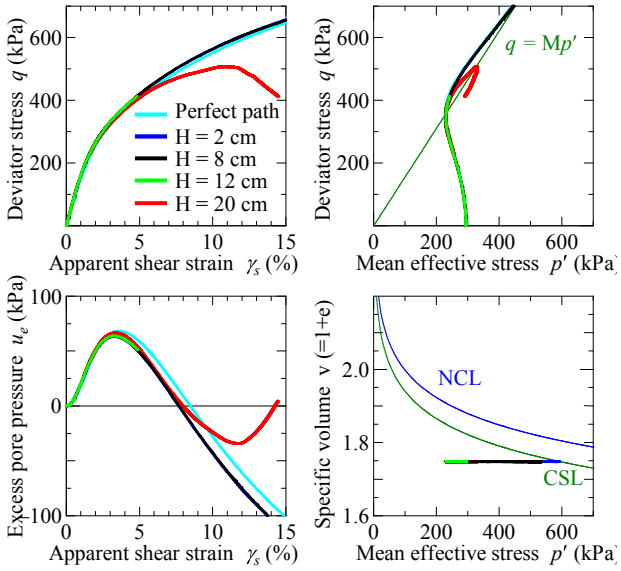


**Fig. 11** Apparent behavior for different heights

**Fig. 11** shows the apparent behavior for four heights comparing with the "Perfect path". Similarly, there are only slight differences among the five responses except the one with H=20 cm. The deviator stress departures from the others at 6% apparent shear strain and then undergoes a sudden decrease at about 12% apparent shear strain. From the distribution of shear strain (omitted), the torsion failure is observed at two ends. Generally, it is thought that in order to eliminate the end friction, specimens with greater heights are preferred, which also corresponds to the deviation results in **Fig. 10**. However, the end failure shown above illustrates that there should be a critical height for the given thickness and diameter to prevent the end failure and the height should be chosen carefully in practical experiments.

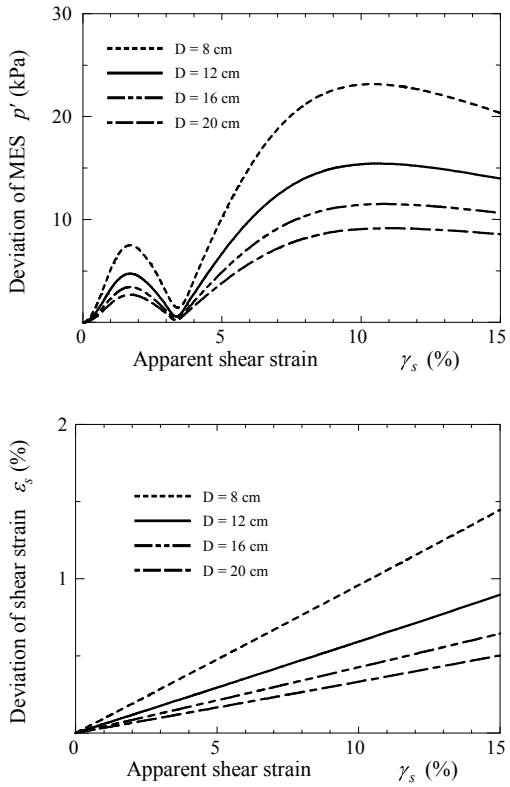


**Fig. 12** Non-uniformity of mean effective stress $p'$ and shear strain $\varepsilon_s$

### 3.2.3 Influence of outer diameter

The deviations of mean effective stress and shear strain against the apparent shear strain are demonstrated in **Fig. 12**. As predicted using isotropic linear elastic analysis by Height et al.[1)], the same tendency that the smaller the curvature is, the smaller the deviation is can be acquired. In addition, the decreasing rate of the non-uniformities is becoming lower and lower until the point where even if the outer diameter is large enough, there are no significant decreases in the non-uniformity.

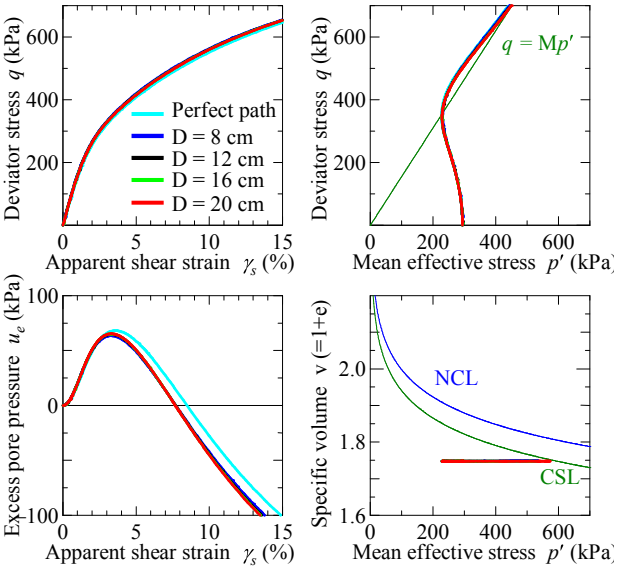


**Fig. 13** Apparent behavior for different outer diameters

**Fig. 13** gives the apparent behavior for four outer diameters comparing with the "Perfect path". From the figure, the only difference between the "Perfect path" and responses at four various outer diameters is the excess pore water pressure, which comes from the wall thickness as clarified in **Fig. 9**. There is no influence of non-uniformity on the apparent behavior as seen from **Figs. 8**, **11** and **13**. To sum up the apparent behaviors at different wall thicknesses, heights and outer diameters, there is almost no difference except excess pore water pressure due to wall thickness and the non-uniformities existing inside the specimen have no effect on the apparent behavior. One of the possible reasons is that the ideally equal torque rate is applied on the top for each node in numerical calculations, which

represents the perfectly frictional contact and no relative displacement between the pedestal and the top surface of specimen. However, such a strict constraint condition cannot be satisfied precisely in practical experiments, which results in slight differences in effective stress path between various specimen geometries .

## 4. Conclusions

A series of monotonic undrained hollow cylinder shear tests (HCT) has been carried out numerically taking into consideration of the influence of specimen geometries on non-uniformities and apparent behaviors. The conclusions are as following:

1) The feasibility of simulating the 3D HCT was proved by treating the specimen as a boundary value problem. The non-uniformities of shear strain, excess pore water pressure and overconsolidation were presented. For the different torque applications, the apparent behavior showed no significant difference while the specific volume change indicated a slight difference due to the variation of end constraints.

2) As for the specimen geometries, the focus was put on the extent of non-uniformity and the influence of curvature and end constraints on such a non-uniformity. A new evaluating method was proposed for the non-uniformity, which is suitable for 3D analyses. It was found that when the cylinder wall thickness became smaller, the non-uniformity also decreased correspondingly; the same decreasing tendency of non-uniformities could also be observed as the specimen height became greater and the specimen outer diameter became larger.

3) In addition, the response of a single 3D element with the same boundary conditions as the 3D hollow cylinder, which is called “Perfect path” and represented a completely uniform deformation field, was computated to investigate the influence of non-uniformities on the apparent behavior. The results indicated that except the case with thinnest wall thickness, there were slight deviations from the “Perfect path”. However, the deviations were so small that it could be acceptable. Moreover, according to the apparent behavior, there should be a critical height for the given wall thickness and outer diameter to prevent the possible end failures, even though the increase of height could reduce the effect of end constraints.

## 5. Further study

1) There is no additional vertical load in the calculation and the stress path in this paper follows $p'$=const, $b$=0 and $P_i$=$P_o$. Simulations under more general stress paths should be carried out to extend the constitutive model and verify the constitutive response considering principal stress orientations and principal rotations.

2) A cyclic torque loading with torque control or displacement control should also be designed to investigate the influence of anisotropy on liquefaction and cyclic mobility in soils.

3) The shear band/strain localization phenomenon observed in most practical experiments is anticipated to be represented by introducing the initial geometrical imperfection.

## ACKNOWLEDGEMENT

This work was supported by MEXT (The Ministry of Education, Culture, Sports, Science and Technology) KAKENHI (Grant-in-Aid for Scientific Research (S)) 20126012.

## Reference

1) Height, D. W., Gen, A. and Symes, M. J.: The development of a new hollow cylinder apparatus for investigating the effects of principal stress rotation in soils, Géotechnique, Vol. 33, No. 4, pp. 355-383, 1983.
2) Lade, P. V., Nam, J. and Hong, W. P.: Shear banding and cross-anisotropic behavior observed in laboratory sand tests with stress rotation, Can. Geotech. J., Vol. 45, pp. 74-84, 2008.
3) Nakata, Y., Hyodo, M., Murata, H. and Yasufuku, N.: Flow deformation of sands subjected to principal stress rotation, Soils and Foundations, Vol. 38, No. 2, pp. 115-128, 1998.
4) Sayao, A. and Vaid, Y. P.: Effect of intermediate principal stress on the deformation response of sand, Can. Geotech. J., Vol. 33, pp. 822-828, 1996.
5) Lade, P. V.: Torsion shear apparatus for soil testing, Symp. On Laboratory Shear Strength of Soil, ASTM STP 740, pp. 145-163, 1981.
6) Sayao, A. and Vaid, Y. P.: A critical assessment of stress non-uniformities in hollow cylinder test specimens, Soils and Foundations, Vol. 31, No. 1, pp. 60-72, 1991.
7) Asaoka, A., Nakano, M. and Noda, T.: Soil-water coupled behavior of saturated clay near/at critical state, Soils and Foundations, Vol.34, No.1, pp.91-105, 1994.
8) Asaoka, A. and Noda, T.: Imperfection-sensitive bifurcation of Cam-clay under plane strain compression with undrained boundaries, Vol.35, No.1, pp.83-100, 1995.
9) Xu, B., Nakai, k., Noda, T., Kishimoto, M., and Takaine, T.: Effect of inertia term on the 3D undrained triaxial compression test, Proc. of 46th JGS Annual Meeting., 2011.
10) Jin, Y., Ye, B. and Zhang, F.: Numerical simulation of sand subjected to cyclic load under undrained conventional triaxial test, Soils and Foundations, Vol.50, No.2, pp.177-194, 2010.
11) Gens, A. and Potts, D. M.: Formulation of quasi-axisymmetric boundary value problems for finite element analysis, Engineering Computations, Vol.1, No. 2, pp.144-150, 1984.
12) Asaoka, A., Nakano, M. and Noda, T. : Superloading yield surface concept for highly structured soil behavior, Soils and Foundations, Vol.40, No.2, pp.99-110, 2000.
13) Asaoka, A., Noda, T., Yamada, E., Kaneda, K., and Nakano, M.: An elasto-plastic description of two distinct volume change mechanisms of soils, Soils and Foundations, Vol.42, No.5, pp.47-57, 2002.
14) Asaoka, A., and Noda, T.: All soils all states all round geo-analysis integration, International Workshop on Constitutive Modelling - Development, Implementation, Evaluation, and Application, pp.11-27, 2007.
15) Noda, T., Asaoka, A. and Nakano, M.: Soil-water coupled finite

deformation analysis based on a rate-type equation of motion incorporating the SYS Cam-clay model, Soils and Foundations, Vol.48, No.6, 771-790, 2008.

**APPENDIX-A**

In practical process, the entire specimen is regarded as a single element with stress and strain components derived from an assumption of linear elastic constitutive with infinitesimal deformation. Eqs. (A-1) and (A-2) present the average stress and strain due to non-uniformity, where $R_o$ $R_i$ are the external and internal radius; $u_o$ $u_i$ are the inner and outer displacement; $\Delta H$ $\Delta\theta$ are the increment in vertical and circumferential direction.

$$\begin{aligned}
\sigma_{zz} &= \frac{F_z + \pi R_o^2 P_o - \pi R_i^2 P_i}{A} \\
\sigma_{rr} &= \frac{P_o R_o + P_i R_i}{R_o + R_i} \\
\sigma_{\theta\theta} &= \frac{P_o R_o - P_i R_i}{R_o - R_i} \\
\sigma_{\theta z} &= \frac{3T_\theta}{2\pi(R_o^3 - R_i^3)}
\end{aligned} \tag{A-1}$$

$$\begin{aligned}
\varepsilon_{zz} &= -\frac{\Delta H}{H} \\
\varepsilon_{rr} &= -\frac{u_o - u_i}{R_o - R_i} \\
\varepsilon_{\theta\theta} &= -\frac{u_o + u_i}{R_o + R_i} \\
\varepsilon_{\theta z} &= \frac{\Delta\theta\left(R_o^3 - R_i^3\right)}{3H(R_o^2 - R_i^2)}
\end{aligned} \tag{A-2}$$

$$\begin{aligned}
p &= -\frac{(\sigma_{zz} + \sigma_{rr} + \sigma_{\theta\theta})}{3} \\
p' &= p - u_e \\
q &= \sqrt{\frac{3}{2}\left\{\begin{matrix}(\sigma_{zz} - p)^2 + (\sigma_{rr} - p)^2 \\ +(\sigma_{\theta\theta} - p)^2 \\ +2{\sigma_{\theta z}}^2\end{matrix}\right\}}
\end{aligned} \tag{A-3}$$

**APPENDIX-B**

In **Fig. C-1**, the triangle represents the displacement constraint in the direction. As can be seen, there are three symmetrical planes consisting of plane 1243, plane 3487 and plane 1375; constant stresses $\sigma_{xx}$ , $\sigma_{yy}$ and $\sigma_{zz}$ are applied correspondingly. The shear stress is represented by applying a constant velocity on plane 2486.

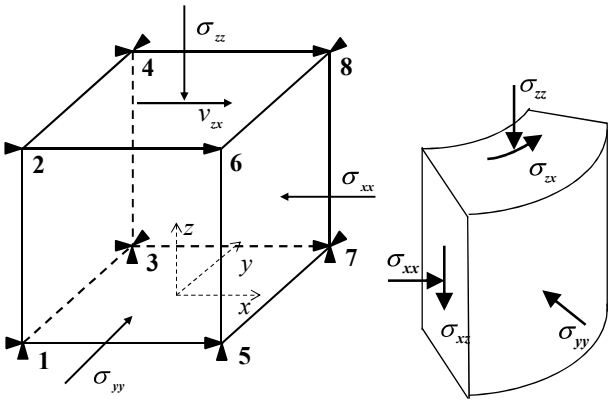


**Fig. C-1** Boundary conditions for one 3D element with a uniform deformation field